Nano Research
2023, 16(4): 4775–4785

ISSN 1998-0124 CN 11-5974/O4
https://doi.org/10.1007/s12274-022-5259-5

Research Article

High-entropy layered oxides nanosheets for highly efficient photoelectrocatalytic reduction of CO_2 and application research

Xuefei Liu[1], Xiaoyan Wang[1], Beibei Yang[1], Junzheng Zhang[1], and Jun Lu[1,2] (✉)

[1] *State Key Laboratory of Chemical Resource Engineering, Beijing University of Chemical Technology, Beijing 100029, China*
[2] *Beijing Advanced Innovation Center for Soft Matter Science and Engineering, Beijing University of Chemical Technology, Beijing 100029, China*

Received: 27 July 2022 / **Revised:** 29 October 2022 / **Accepted:** 31 October 2022

ABSTRACT

High-entropy oxides receive significant attention owing to their "four effects". However, they still suffer from harsh construction conditions such as high temperature and high pressure and present a block-like structure. Herein, in this work, Ni-Mn-Cu-Co-Fe-Al high-entropy layered oxides (HELOs) with a layered nanosheet structure were constructed by a simple pathway of topological transformation under relatively low temperature (300 °C) with six-membered Ni-Mn-Cu-Co-Fe-Al layered double hydroxides (LDHs) precursors, which exhibited an outstanding activity and excellent selectivity for CO_2 photoelectroreduction (obtaining the highest carbon monoxide yield of 909.55 μmol·g^{-1}·h^{-1} under −0.8 V vs. reversible hydrogen electrode (RHE), which is almost twice that of pure electrocatalysis). In addition, the charging voltage of a photo-assisted Zn-CO_2 battery with HELOs as electrode was reduced from 2.62 to 2.40 V; the discharging voltage of the battery was increased from 0.51 to 0.59 V with the assistance of illumination. The improvement of round-trip efficiency of the battery indicates that light played a positive role in both the charging and discharging processes. This study not only lays an important foundation for the development of high-entropy oxides but also expands their application in the field of photoelectrochemistry.

KEYWORDS

high-entropy layered oxides (HELOs), CO_2 reduction, layered double hydroxides (LDHs), photoelectrocatalytic

1 Introduction

As one of the energy conversion strategies, photoelectrocatalytic technology [1, 2] exerts a far-reaching influence on CO_2 consumption. Several efforts have been devoted to conversion of CO_2 to commodity chemicals via photoelectrocatalytic reduction as it combines the advantages of photocatalytic reduction and electrocatalytic reduction. However, one major obstruction of the aforementioned measure is the limited valued chemicals production instead of generating electricity simultaneously. Therefore, metal-CO_2 batteries have been extensively developed due to the advantage of producing valued chemicals and generating electricity simultaneously, especially in recent years. Among them, the Zn-CO_2 battery has attracted researchers' attention because it does not require harsh (such as anhydrous and oxygen-free) conditions and could utilize the proton-coupled electron transfer mechanism to facilitate flexible CO_2 electrochemistry [3]. Additionally, the sluggish kinetics of many reactions (such as CO_2 reduction reaction, oxygen reduction reaction, and oxygen evolution reaction) can be facilitated by the introduction of solar energy, which has been confirmed by massive research [4–6]. Inspired by above researches, photo-assisted Li-CO_2 batteries were realized by Professor Xu [7, 8], which promote the discharge and charge processes and thus improve the energy efficiency greatly. However, one major obstacle of Li-CO_2 batteries for scale development is the harsh conditions (anhydrous and oxygen-free), and thus they cannot satisfy the requirements of a protonated environment. Fortunately, Zn-CO_2 batteries take advantage of the proton-coupled electron transfer mechanism to enhance CO_2 reduction reaction [3, 9].

As one of the most potential metals for CO_2 reduction, copper can strongly adsorb carbon monoxide and has a weaker adsorption force with H, thus encouraging the CO or formic acid generation while preventing the formation of H_2 [10–14]. However, the application of Cu alone still suffers from the problems of activity and product selectivity. Therefore, it would be appealing to combine Cu with other metals into nanomaterials. High-entropy materials (HEMs), which include four or even more metals, have been discovered in recent years [15, 16]. Hu has made many efforts and achieved relevant results for high-entropy materials [17–25]. Because of their excellent performance, HEMs have received widespread attention. The excellent performance can be summarized as follows: the high entropy effect, the lattice distortion effect, the delayed diffusion effect, and the cocktail effect [26, 27]. A variety of elements with similar proportions were adopted to be fully mixed and highly dispersed, so as to achieve a high-performance material. As HEMs [26], high-entropy alloys (HEAs) [28, 29], high-entropy oxides (HEOs) [30, 31], high-entropy sulfides [32, 33], high-entropy phosphides [34, 35], and high-entropy (oxy)hydroxides [36] have all been successfully prepared, and the application field is also gradually expanding from catalysis to energy storage (such as oxidation–reduction reaction (ORR), oxidation evolution reaction (OER), CO_2 reduction reaction (CO_2RR), and CO reduction reaction

Address correspondence to lujun@mail.buct.edu.cn

(CORR)). Singh [37] for the first time reported HEMs for CO_2 reduction. Since then, the literature related to employing HEMs for CO_2 reduction has gradually increased [33, 37, 38]. The similarities of the studies were putting emphasis on electrocatalytic or photocatalytic CO_2RR.

At present, the conventional preparation method of HEOs is still far from satisfactory due to the harsh conditions such as high temperature or high pressure and the limited exposed active sites as well as poor activity [39]. Therefore, it would be appealing if we can attain mild preparation conditions, high dispersion, and rich exposed active sites in the preparation of HEOs. As one of typical layered materials, layered double hydroxides (LDHs) have been researched broadly due to the superior performance of combining a large number of elements and can be modified by calcination or other methods. Thus, they can be a superior precursor to obtain high-entropy layered oxides (HELOs) and meanwhile address the obstacles of poor active sites and a smaller specific surface area. LDHs have been adopted to prepare high-entropy oxides with the low-temperature plasma strategy for 5-hydroxymethylfurfural electrooxidation [39]. However, considering the limitations and complexities of plasma strategy, an effortless and mild strategy of air atmosphere calcination was developed for preparing HELOs based on precursor LDHs, which avoids the harsh conditions of high temperature and high pressure without redundant procedures. To the best of our knowledge, reports on employing high-entropy oxides as photoelectric materials for assembling photo-assisted systems and CO_2 photoelectroreduction remain undeveloped.

Hence in this work, we prepared hexabasic HELOs (Ni, Mn, Cu, Co, Fe, and Al) with hexabasic LDHs precursors through calcination under a relatively low temperature (T = 300 °C), which present a layered structure with exposed active sites. Furthermore, the precursor LDHs were then acquired for comparison. Then CO_2 photoelectroreduction was performed, and photo-assisted aqueous Zn-CO_2 batteries were assembled with aforementioned hexabasic HELOs as photoelectric material.

2 Experimental section

2.1 Preparation of materials

In this work, hydrated nitrates were applied as the metal salt source, such as manganese nitrate tetrahydrate and cobalt nitrate hexahydrate. Reagents such as sodium hydroxide, sodium carbonate, zinc acetate, potassium bicarbonate, and potassium hydroxide were used in this study, and consumables such as bipolar membrane and Nafion membrane were used in the H-type cell. Reagents not mentioned in this work were directly used in the experimental process. The experimental water was self-made.

2.2 Construction of six-membered LDHs precursors

Equimolar amounts (8 mmol) of nickel-manganese-copper-cobalt-iron-aluminum metal source were transferred and dissolved in 80 mL of deionized water as solution A. 92 mmol of sodium hydroxide and 32 mmol of anhydrous sodium carbonate were dissolved in 80 mL of deionized water as solution B. 20 mL of deionized water was transferred to a four-neck beaker as the bottom liquid. The four-necked flask was under mechanical stirring, and then the four-necked flask was placed in a constant temperature water bath at 75 °C. During the whole stirring process, A and B solutions are then added dropwise simultaneously. The specific operation was as follows: adjusting the injection pump with a certain flow rate for solutions A and B, strictly controlling the pH during the process of dropping to keep the pH of the suspension in the four-necked flask always at 9–10, stopping operation until solution A or solution B was completely consumed, and then sealing the four-necked flask for 8 h of reaction.

At the end of the reaction, the precursors were washed with water and ethanol several times so that the final pH was approximately neutral. Then they were dried with freeze-drying apparatus for 12 h. The powder of LDHs precursors was formed successfully.

2.3 Construction of six-element HELOs

A certain amount of six-element (nickel-manganese-copper-cobalt-iron-aluminum) LDHs precursors were transferred to a crucible and calcined at 300 °C for 8 h under air atmosphere in a muffle furnace. The heating rate was set as 10 °C·min^{-1}. After that, the sample was cooled down to room temperature. Then the construction of six-element (nickel-manganese-copper-cobalt-iron-aluminum) HELOs was completed. A schematic diagram of the construction of six-membered HELOs is shown in Fig. 1(a).

2.4 Construction of five-element HELOs

Six kinds of five-membered LDHs (respectively minus one of the metal elements), 80 mmol of sodium hydroxide, and 32 mmol of anhydrous sodium carbonate were used in this process. The method was same to the construction scheme of six-membered LDHs precursors, and other conditions remained unchanged. Then the five-membered LDHs precursors were transformed into the corresponding five-membered HELOs with the above scheme, respectively.

2.5 Characterization of materials

X-ray diffraction (XRD), scanning electron microscopy (SEM), high-resolution transmission electron microscopy (HRTEM), energy dispersive spectroscopy (EDS), element mapping, X-ray photoelectron spectroscopy (XPS), and other characterizations were performed to analyze the basic information of materials such as element information, morphology, and other properties. Photoluminescence (PL) spectroscopy and ultraviolet–visible (UV–vis) diffuse reflectance spectroscopy (DRS) were utilized to examine the optical properties of LDHs precursors and HELOs. Electrochemical impedance spectroscopy (EIS) and other photoelectronic characterizations were performed to examine the photoelectronic properties of materials.

2.6 Performance test of photoelectric reduction of CO_2

The CO_2 photoelectroreduction performance test was carried out in a gas-tight H-type photoelectrolytic cell separated by a Nafion 117 membrane. 25 mL of 0.5 M $KHCO_3$ solution was adopted as the catholyte, while 25 mL of 1 M KOH solution was used as the anolyte. A three-electrode system was adopted, and HELOs (fluorine-doped tin oxide (FTO) substrate) was adopted as working electrode, Ag/AgCl as reference electrode, and platinum sheet as counter electrode. Potentiostatic i–t reduction was performed on an electrochemical workstation. The photoelectrochemical CO_2 reduction was carried out at room temperature, and high-purity CO_2 gas was passed into the cathode chamber for 30 min, and then photoelectrochemical CO_2 reduction was carried out under different potentials. The reaction time was 7200 s. The gaseous product was taken every hour by a gas chromatographic syringe, and then qualitative and quantitative analysis was made by gas chromatography. Gaseous products were detected using a gas chromatograph (GC7970, nickel reformer, nitrogen as carrier gas) equipped with a flame ionization detector and a chromatographic column (TDX-01). Liquid

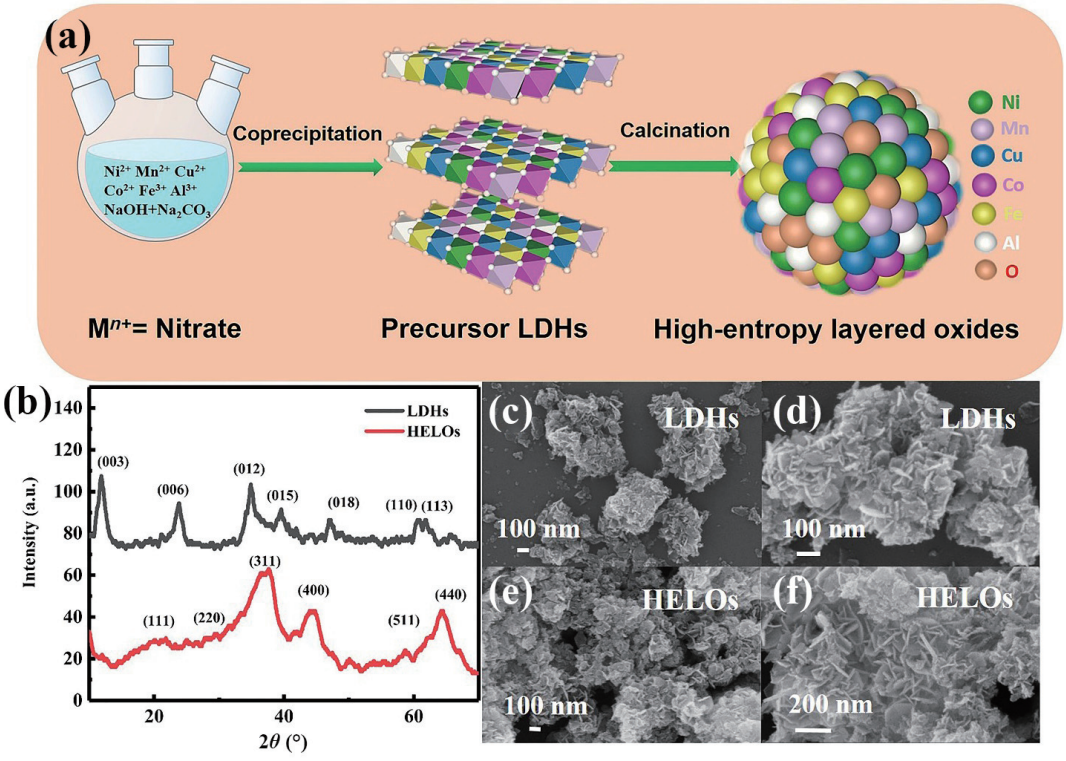

Figure 1 (a) Schematic diagram of the construction of HELOs. (b) XRD patterns of HELOs and precursor LDHs. (c) and (d) SEM images of precursor LDHs. (e) and (f) SEM images of HELOs.

products were identified and quantified using a Bruker Avance III 400 MHz HD instrument with ^{1}H NMR measurement capability. This procedure used dimethyl sulfoxide (DMSO) as an internal standard to quantify the liquid products of electrolysis at each given potential. In this study, a 300 W xenon lamp was utilized as the light source for the photo-assisted system. Since the running time of cyclic performance test was so long, the long-term utilization of the xenon lamp would affect the light intensity and stability. Herein a light-emitting diode (LED) lamp matched with the rotating disk electrode (RDE) in photoelectric performance characterization was utilized in the photo-assisted battery test.

2.7 Assembly of photo-assisted Zn-CO_2 batteries

35 mL of 0.5 M $KHCO_3$ solution and 25 mL of 1.0 M KOH solution added with 0.02 M $(CH_3COO)_2Zn$ were used as catholyte and anolyte, respectively. The photo-assisted aqueous Zn-CO_2 battery consisted of HELOs cathode and a zinc sheet (2 cm × 5 cm) anode. The two chambers in an air-tight H-type electrolytic cell with a quartz window were separated by bipolar membranes (maintaining pH of the solutions at both chambers). Then the performance test of the photo-assisted Zn-CO_2 battery was carried out on the battery test system (LANHE CT2001A).

3 Results and discussion

As shown in Fig. 1(b), the XRD pattern of precursor demonstrates that hexabasic (Ni, Mn, Cu, Co, Fe, and Al) LDHs were prepared successfully, and the peaks appearing at 11.6°, 23.3°, 34.7°, 39.2°, 46.7°, 60.3°, and 61.7° agree well with the (003), (006), (012), (015), (018), (110), and (113) planes of LDHs. The HELOs were attained by calcination of LDHs precursors at 300 °C for 8 h under air atmosphere. The major peaks displayed at 19.0°, 31.3°, 36.8°, 44.8°, 59.4°, and 65.23° as shown in Fig. 1(b) can be indexed to (111), (220), (311), (400), (511), and (440) planes of HELOs. The existence of this single phase confirms the successful construction of high-entropy oxides. The detailed morphological information of precursor LDHs and HELOs was characterized by SEM as displayed in Figs. 1(c)–1(f). It can be seen that the six-element precursor LDHs (Figs. 1(c) and 1(d)) still maintained the layered structure being similar to the binary and ternary LDHs. In other words, the morphology and structure of LDHs will be not affected by the quantity of metal elements, which is also consistent with the results obtained by XRD. After relatively low temperature calcination under air atmosphere, the morphology and structure of the six-membered HELOs shown in Figs. 1(e) and 1(f) were obtained. By comparing SEM images of HELOs and precursor LDHs, it can be clearly found that the morphology and structure of HELOs were maintained well without obvious agglomeration or other morphology changes, which still held a lamellar nanosheet structure. The larger lamellar structure can provide abundant active sites, which is beneficial for catalytic reaction. Simultaneously, as a promising approach, constructing HELOs by LDHs precursors through calcination under air atmosphere can be extended to other layered materials, which provides avenues for other multi-component materials (such as metal–organic framework) to convert into high-entropy oxides.

For the sake of studying the size and other information (such as lattice size) of HELOs nanosheets, HRTEM was performed. The HELOs were highly dispersed as shown in Figs. 2(a) and 2(b). This result demonstrates that the nanosheet size of HELOs was about 100 nm as displayed in Fig. 2(c). As shown in Fig. 2(c), in addition to the hexagonal shape of the nanosheets, it can be seen that the surface of the nanosheets is uniform and presents white holes, which is not similar to the uniform precursor LDHs (as shown in Fig. S1 in the Electronic Supplementary Material (ESM)) on the surface of the nanosheets. This difference is mainly caused by the process of calcination in an air atmosphere. In other words, some carbonates and other substances are removed from the laminate during the calcination process to realize topological conversion into HELOs. The smaller size and high dispersion of HELOs favor rich active sites exposed and support more absorption sites for CO_2 reduction reaction. The lattice size of 2.05 Å was characterized as shown in Fig. 2(d), corresponding to

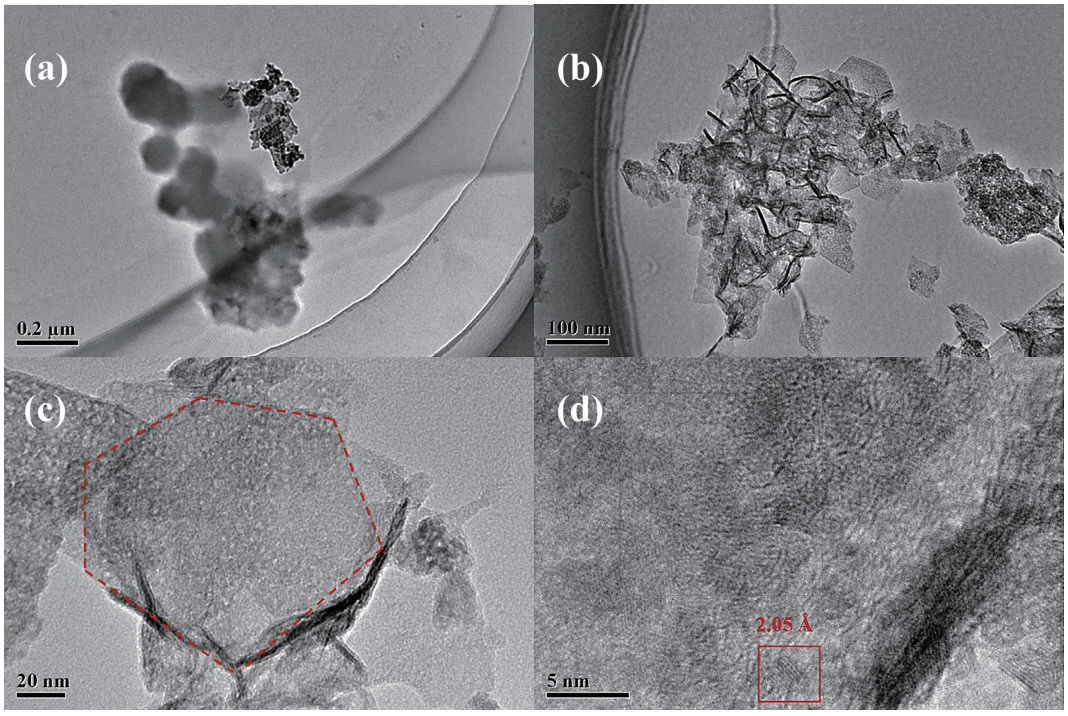

Figure 2 (a)–(d) HRTEM images of HELOs.

the (400) plane of HELOs, in line with the XRD results, which validates the successful construction of HELOs again.

The content and distribution of several metal elements and oxygen element of samples were further investigated by element mapping and energy dispersive X-ray spectroscopy (EDX). The results illustrate that the elements (Ni, Mn, Cu, Co, Fe, Al, and O) all dispersed uniformly as shown in Fig. 3. In addition, according to the analysis results of EDS element content, oxygen element accounts for the largest proportion of 71.66%, which is reasonable for oxides. The EDX results demonstrate that all six metal elements were present in HELOs as shown in Fig. 3. Furthermore, the proportions of various metals in LDHs and HELOs were characterized by inductively coupled plasma (ICP). As shown in Table 1, ICP results show that there is no change in the proportions of several metals after the conversion of LDHs to HELOs. In addition, there is little difference in the proportions of several metals, except for aluminum, which accounts for a less proportion in the synthesized LDHs mainly because it is an amphoteric metal. Thus the proportion of aluminum element in HELOs is relatively small.

Fourier transform infrared spectroscopy (FTIR) was adopted to characterize the functional group information of the materials, and the results are shown in Fig. 4. The vibrational peaks appearing at 3447 and 1632 cm^{-1} were assigned to νO–H on the laminate. The precursor LDHs and HELOs all exhibit this vibration. The corresponding vibrational peaks at 1383, 849, and 599 cm^{-1} were assigned to νCO_3^{2-}, which was detected because the layer of precursor LDHs contained carbonate and sodium carbonate was employed in precursor synthesis process. The vibrational peak at 503 cm^{-1} is assigned to the M–O–M group, the vibrational peak of the metal–oxygen bond, which was present in HELOs but did not appear in the precursor LDHs. Owing to abundant M–O bonds contained in high-entropy oxides, it is reasonable that there are abundant M–O–M bonds contained in HELOs. This result adds a new reference evidence for the successful construction of HELOs.

For the sake of further studying the elemental composition and chemical state changes before and after material transformation, XPS was applied to compare the chemical valence changes of elements in HELOs and precursor LDHs. As shown in Fig. 5, compared to precursor LDHs, no significant difference appears in the XPS spectra of divalent metal elements and trivalent metal elements in HELOs. As shown in Fig. 5, in detail, two peaks appear in the XPS diagram of Ni 2p at 855.06 and 872.64 eV. Combined with the positions of the two satellite peaks, it is inferred that the nickel element is Ni^{2+}. Compared with the precursor LDHs (855.93 and 873.53 eV), there is only a slight shift in the lower binding energy direction, indicating that the metal valence state of nickel does not change significantly. The peaks located at 641.6, 643.06, and 645.47 eV in the Mn 2p XPS spectrum of HELOs (Fig. 4(b)) can be assigned to Mn^{2+}, Mn^{3+}, and Mn^{4+}, respectively [40, 41]. The corresponding XPS peaks of Mn 2p in LDHs appear at 640.77, 642.1, and 643.75 eV. Compared with the XPS peaks of Mn 2p in precursor LDHs, the peaks in HELOs shift slightly in the direction of high binding energy but overall remain constant. Figure 4(c) shows the XPS spectrum of Cu 2p. In HELOs, the characteristic peaks located at 932.93 and 934.45 eV can belong to Cu^{+} and Cu^{2+}, respectively. Considering Cu $2p_{1/2}$ and satellite peaks, it can be confirmed that the copper metal valence in HELOs is Cu^{+} and Cu^{2+}. The characteristic peaks of the corresponding precursor LDHs can be observed at 932.89 and 934.73 eV, which are similar to those of HELOs. Employing the same analytical method as above, the results reveal that the chemical states of the cobalt (Fig. 4(d)), iron (Fig. 4(e)), and aluminum (Fig. 4(f)) are almost identical without significant change in HELOs compared with precursor LDHs. The only difference is that the ratio of elements in different valence states is different after topological transformation. Combined with the analysis of XRD results, it can be seen that the change appeared in crystal phase between precursor LDHs and HELOs rather than in the valence states of the elements, whether divalent metal elements or trivalent metal elements. That is to say, there is no apparent change appearing in the valence states of elements due to the calcination process. This result can be observed more intuitively in the full XPS spectrum, as shown in Fig. 6.

Above characterizations were adopted to analyze the internal structure and morphology of the material. For photoelectric catalysts, the excellent optical properties promote light absorption

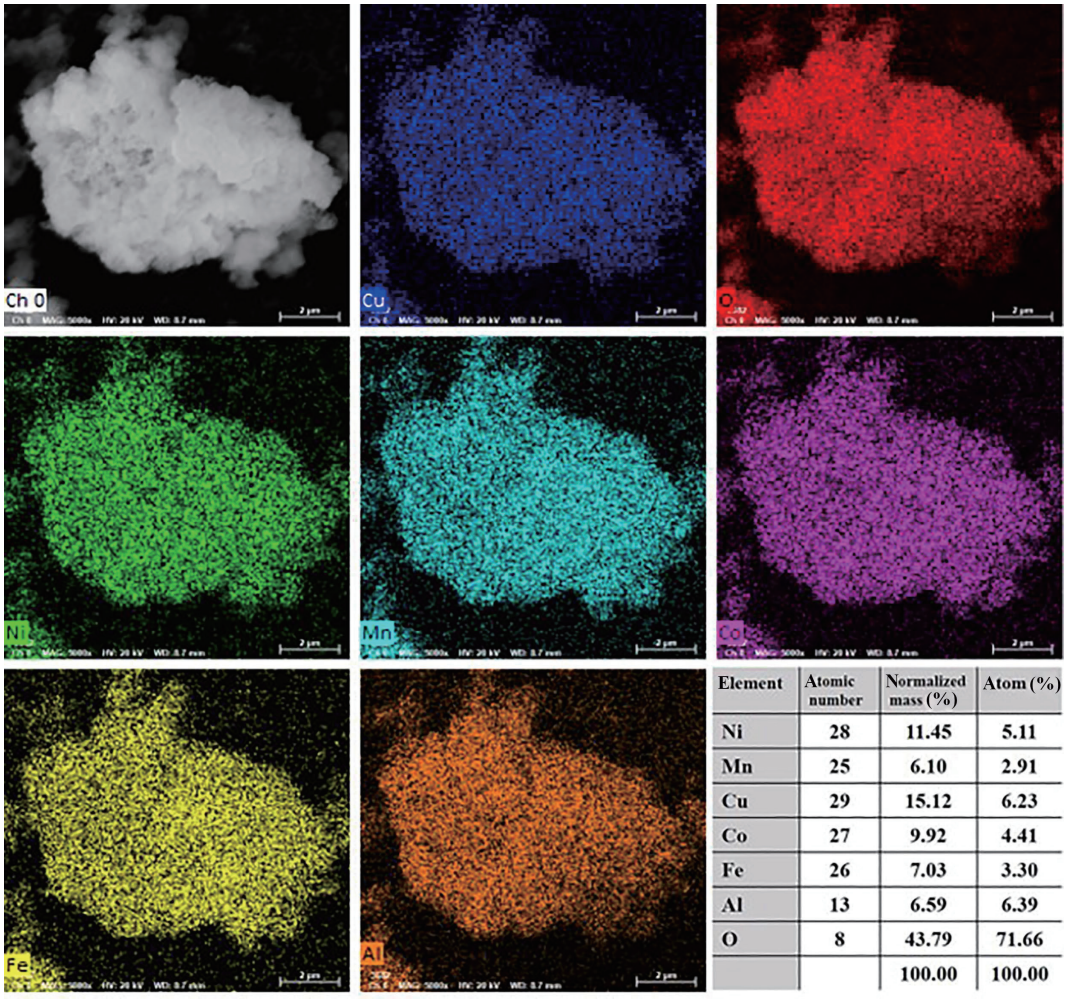

Element	Atomic number	Normalized mass (%)	Atom (%)
Ni	28	11.45	5.11
Mn	25	6.10	2.91
Cu	29	15.12	6.23
Co	27	9.92	4.41
Fe	26	7.03	3.30
Al	13	6.59	6.39
O	8	43.79	71.66
		100.00	100.00

Figure 3 Element mapping and EDX analysis of HELOs.

Table 1 ICP results of precursor LDHs and HELOs

Samples	Ni (%)	Mn (%)	Cu (%)	Co (%)	Fe (%)	Al (%)
LDHs	17.96	17.93	20.42	17.71	15.92	10.05
HELOs	18.04	17.69	19.78	17.65	16.47	10.37

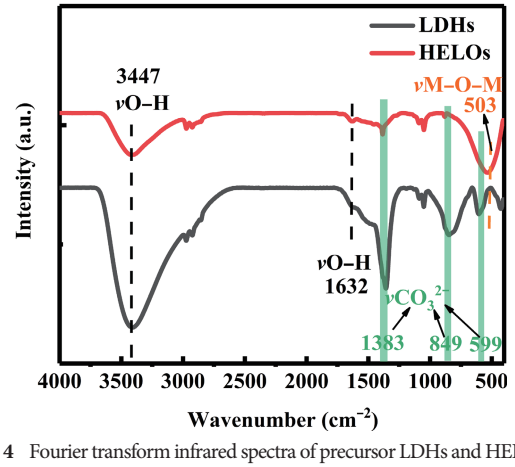

Figure 4 Fourier transform infrared spectra of precursor LDHs and HELOs.

and carrier separation, which enhance the redox reaction actively. Therefore, optical performance comparison and analysis were performed by PL and UV–vis DRS (Fig. 7). Figure 7(a) shows the UV–vis DRS spectra of the precursor LDHs and HELOs, which are utilized to demonstrate the difference in light absorption properties. It can be clearly found that the light absorption performance of HELOs is better than that of its precursor LDHs in both the ultraviolet absorption region (200–400 nm) and the visible light region (400–800 nm), indicating that the resulting high-entropy oxides maintain the lamellar structure required for catalysis and obtain better light absorption performance. This may be attributed to the high mixing of multi-component metals in HELOs, thus facilitating light absorption and the interaction between metal elements. Superior light absorption properties are beneficial to improve the utilization of solar energy in the photoelectric catalytic reaction, thereby further promoting the kinetics of the reaction. For the PL spectrum, the intensity of the PL spectrum is inversely proportional to the separation rate of the photogenerated electron–hole pair, and the low emission intensity is beneficial to the redox reaction. As shown in Fig. 7(b), HELOs possess a lower PL intensity than the precursor LDHs, indicating that HELOs hold better photogenerated electron–hole pair separation ability than the precursor LDHs. Among them, the electrons further participate in the photoelectric reduction of CO_2, which promotes the photoelectric reduction of CO_2. The above result is consistent with the UV–vis DRS result, both indicating that HELOs possess outstanding optoelectronic properties and can be optimal candidates for photoelectric reaction. It is of great importance to examine the photoelectronic properties and CO_2 reduction activity of the materials with an electrochemical

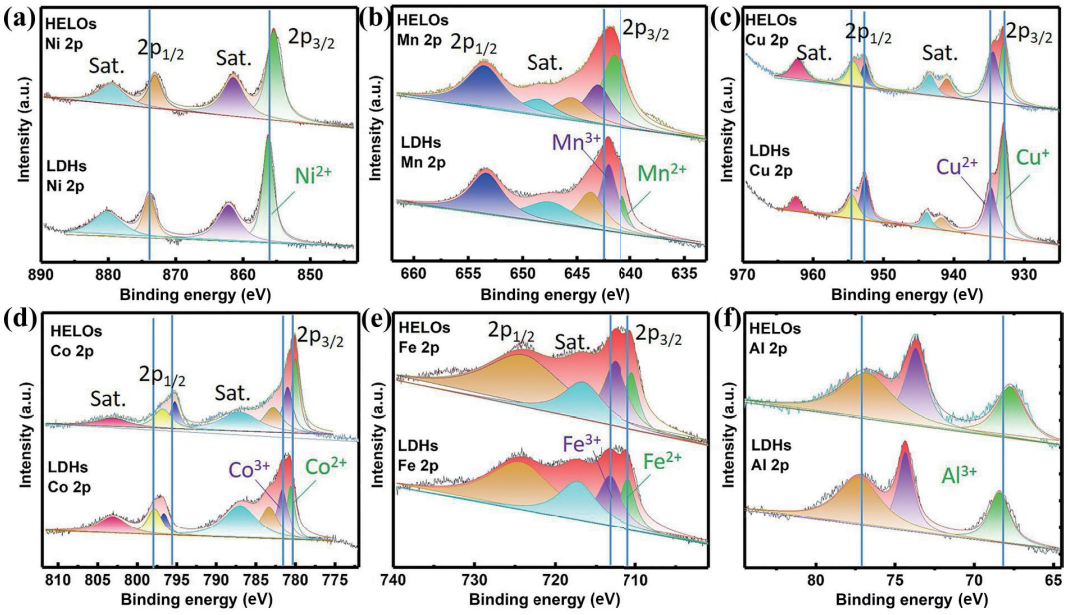

Figure 5 XPS analysis of precursor LDHs and HELOs.

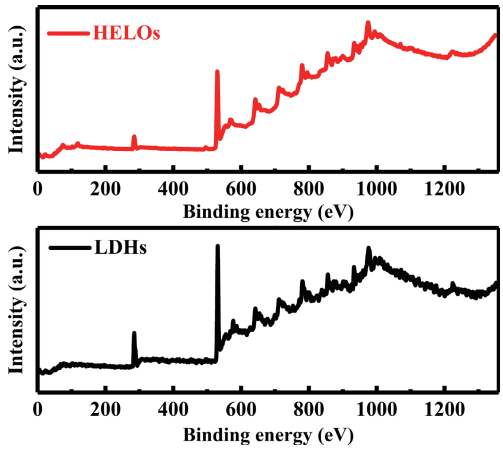

Figure 6 Full XPS spectra of precursor LDHs and HELOs.

workstation. As shown in Fig. 7(c), linear sweep voltammetry (LSV) characterization of HELOs was performed in CO_2-saturated (Ar-saturated) 0.5 M $KHCO_3$ solution with and without irradiation for examining CO_2 reduction activity. It can be seen that the maximum current density (red curve) was obtained at −1.6 V vs. Ag/AgCl in CO_2 atmosphere under illumination. Compared with the Ar atmosphere (no matter whether with illumination or not), the current density of the CO_2 atmosphere without illumination is lower than that of the Ar atmosphere under the same potential such as −1.6 V vs. Ag/AgCl. In other words, HELOs are almost inactive for CO_2 under dark conditions. However, the current density under illumination in CO_2 atmosphere is superior to that in Ar atmosphere under the same potential, indicating that the reactivity of HELOs toward CO_2 is only stimulated with the assistance of light. In detail, in order to further illustrate the central role of light, under the CO_2 atmosphere, the current density of HELOs at −1.6 V vs. Ag/AgCl is determined (nearly 40 $mA{\cdot}cm^{-2}$) under light conditions, which is significantly greater than that in dark conditions (about 5 $mA{\cdot}cm^{-2}$), as shown in the inset of Fig. 7(c). This is the reason why HELOs are selected as photoelectric catalysts for CO_2 reduction rather than electrocatalysts. The better photoelectric activity for CO_2 may be attributed to the remarkable light absorption properties of HELOs and further facilitate the utilization efficiency of solar energy in the first step of the reaction. In addition, the high electron–hole separation rate of HELOs further facilitates CO_2 photoelectroreduction. In order to further examine the photoelectric properties of the material, EIS characterization was employed to evaluate the photogenerated electron–hole pair separation rate of the precursor LDHs and HELOs. The smaller EIS radius indicates that the materials own better electron transport properties, which is beneficial for the photoelectroreduction reaction. As shown in Fig. 7(d), HELOs (green and blue curves) outperform precursor LDHs (red and gray curves) under both irradiation and dark conditions, and HELOs hold the smallest radius under irradiation. The above characterization indicates that HELOs attain the optimal electron transport ability and the optimal separation capability of the photogenerated electron–hole pair under illumination conditions, which proves the superiority of HELOs as the photoelectrocatalysts again. The comprehensive analysis of the above characterization shows that HELOs may be the optimal candidate for photoelectric reduction of CO_2.

Herein, based on above optical and photoelectrochemical analysis, HELOs were employed for photoelectric reduction of CO_2 at different potentials. The products were analyzed by gas chromatography as displayed in Fig. 8. Carbon monoxide is the main product, accompanied by only a trace amount of methane. The maximum carbon monoxide yield of 909.55 $\mu mol{\cdot}g^{-1}{\cdot}h^{-1}$ was achieved under −0.8 V vs. RHE in the photoelectroreduction of CO_2 (Fig. 8(a)), which is almost twice that of pure electrocatalysis (Fig. 8(b)), while the methane yield does not change significantly at different potentials, and the yields are poor. Compared with the electrocatalytic reduction of CO_2 without illumination as displayed in Fig. 8(b), the results imply that the yield of carbon monoxide under pure electrocatalysis is significantly lower than that of photoelectric catalysis (Fig. 8(a)). However, there is an abnormal situation at −1.0 V vs. RHE. The yields of carbon monoxide under electrocatalysis and photocatalysis are close, and even the yield of electrocatalysis (790.95 $\mu mol{\cdot}g^{-1}{\cdot}h^{-1}$) is slightly higher than that of photoelectrocatalysis (742.28 $\mu mol{\cdot}g^{-1}{\cdot}h^{-1}$). The possible reason is that the applied potential is large, so the effect of light is negligible. In other words, electrocatalysis plays a leading role at this high potential. Nevertheless, according to the analysis of the yield results at different potentials, photoelectrocatalysis has a higher yield than electrocatalysis and remarkable selectivity, which is benefited from illumination. It is once again confirmed that

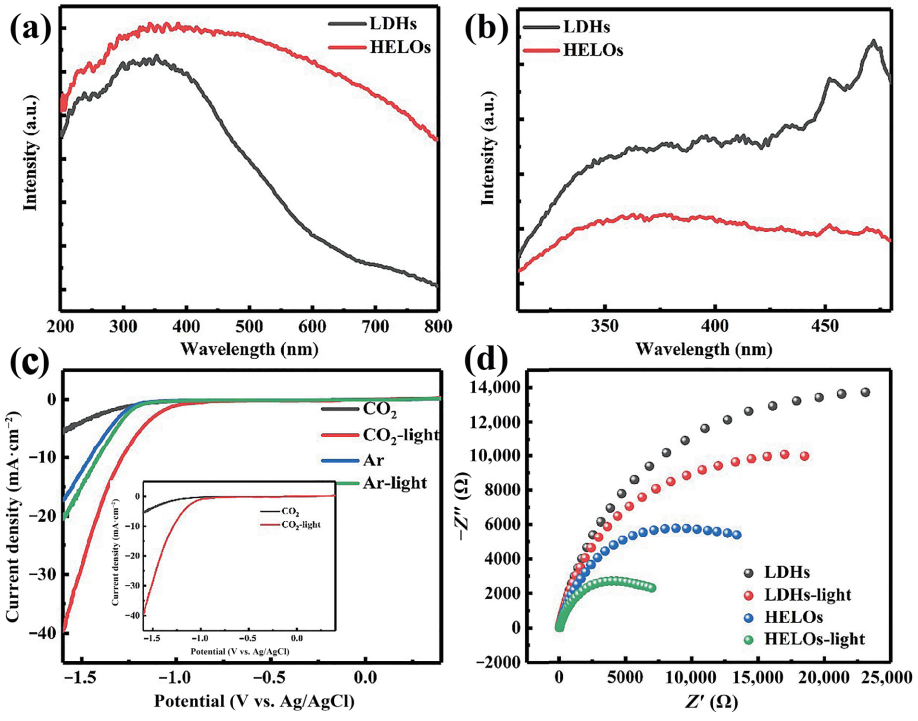

Figure 7 Photoelectric performance characterization of precursor LDHs and HELOs: (a) UV–vis DRS, (b) PL spectroscopy, (c) LSV test under different gas conditions and light/dark conditions, and (d) EIS test.

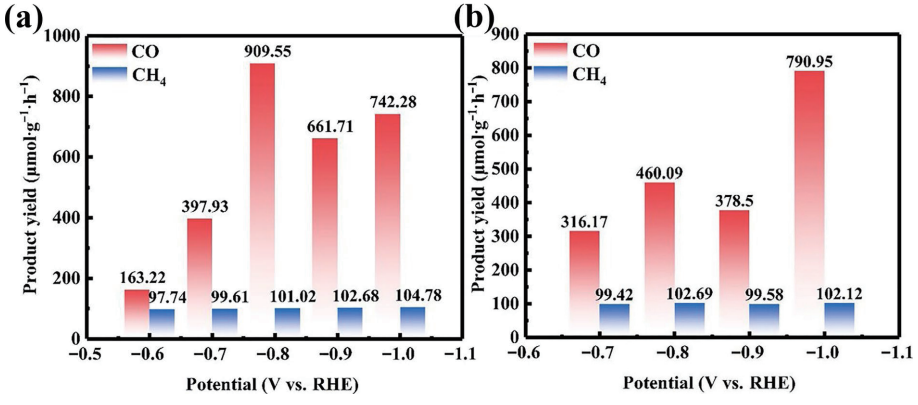

Figure 8 Product yields of HELOs at different potentials: (a) photoelectrocatalytic CO_2RR and (b) electrocatalytic CO_2RR.

HELOs possess excellent photoelectric properties and allow the achievement of carbon monoxide with a superior yield and high selectivity.

To further explore the performance of the photo-assisted Zn-CO_2 battery with HELOs as photocathode, galvanostatic discharge–charge cycling was executed with HELOs as the cathode of the photo-assisted Zn-CO_2 battery. The result is shown in Fig. 9. Fig. 9(a) shows the schematic diagram of the photo-assisted aqueous Zn-CO_2 battery with hexabasic HELOs as photocathode. 0.5 M $KHCO_3$ solution is adopted as the catholyte, and KOH and $(CH_3COO)_2Zn$ are used as the anolyte. The catholyte and the anolyte are separated by a bipolar membrane between two chambers. As can be seen from the schematic diagram (Fig. 9(a)), the cathode material generates electrons and holes under photoexcitation conditions, which further participate in the oxidation and reduction reactions of the cathode, thus promoting the cathodic reaction of the battery. The galvanostatic discharge–charge cycling profiles are shown in Fig. 9(b). Under dark conditions, the charging voltage of the Zn-CO_2 battery was 2.62 V, while that decreased to 2.40 V under illumination. For the discharging voltage of the battery, it was 0.51 V under dark conditions and increased to 0.59 V with the assistance of illumination. Thus, the round-trip efficiency of the photo-assisted Zn-CO_2 battery was improved, indicating that light played a positive role in both the charging process and the discharging process. In addition, the galvanostatic discharge–charge cycling of the photo-assisted Zn-CO_2 battery with HELOs as photocathode can continuously run for about 42 h, as displayed in Fig. 9(c), which is remarkable compared with the reported literature. However, the tendency to promote the discharge reaction is slight and negligible. Therefore, the photocathode of HELOs still suffers from the low activity, and HELOs still remain to be further optimized.

Besides, regarding the mechanism of the Zn-CO_2 battery, since it is still in the initial stage, there is little research on mechanism. As far as we know, the research on the mechanism of photo-assisted Zn-CO_2 batteries still remains undeveloped. In this study, by referring to the mechanism of Zn-CO_2 batteries first proposed by Wang's team, it can be inferred that discharging is the process of reducing CO_2 to generate carbon monoxide and methane, while the charging process is probably the process of water splitting at the cathode. Simultaneously, at the anode, the charging and discharging process is the conversion between metallic zinc and zinc ions. Fig. 9(a) exhibits the possible mechanism clearly.

As an important factor for photoelectric catalysts, stability was assessed by SEM and XPS, which plays a significant role in

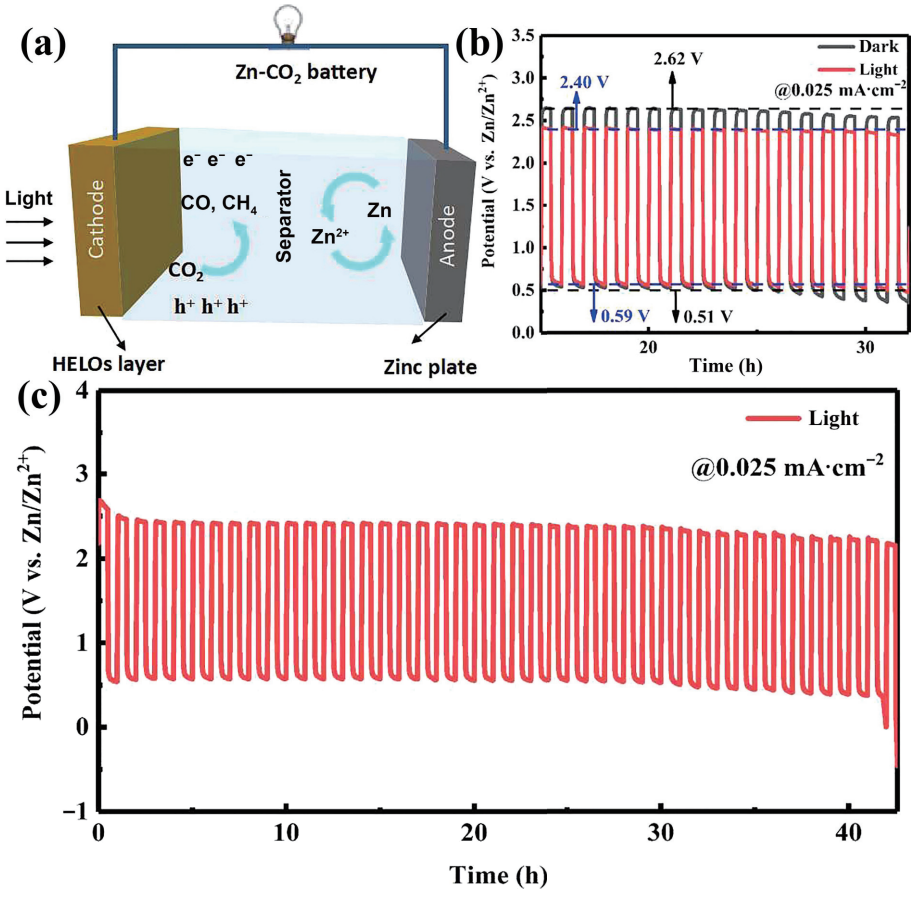

Figure 9 (a) Schematic diagram of photo-assisted aqueous Zn-CO_2 battery with six-element HELOs as photocathode. (b) Charge and discharge profiles of a photo-assisted aqueous Zn-CO_2 battery under light irradiation or without light irradiation. (c) Galvanostatic discharge–charge cycling profiles at 0.025 mA·cm^{-2} with the assistance of light.

evaluating whether the photoelectric catalyst could be produced on a large scale. Usually, there will be obvious phenomena such as agglomeration and accumulation, which limit the catalyst activity and stability. Hence, the SEM characterization was adopted to examine the stability of HELOs. Figure 10 shows the lamellar structure of HELOs after participating in the photoelectroreduction of CO_2. Under different magnifications, the results show that the morphology and structure have not changed significantly, which are similar to those before reaction (Figs. 1(e) and 1(f)). The obvious lamellar structure was still retained, and there was no block accumulation, agglomeration, and other phenomena. It is safe to draw conclusions that HELOs have excellent stability and meet the stability requirements of photoelectric catalysts.

XPS was introduced to compare the change of the valence state of metal elements in the catalyst before and after reaction. Figures 11(a)–11(f) display the XPS spectra of nickel, manganese, copper, cobalt, iron, and aluminum of the HELOs after the reaction, respectively. As shown by the Ni 2p XPS spectrum after reaction in Fig. 11(a), the peaks appearing at 855.04 and 872.59 eV correspond to Ni $2p_{3/2}$ and Ni $2p_{1/2}$, respectively, and those at 861.21 eV and 879.82 eV are corresponding satellite peaks. This group of peaks is attributed to Ni^{2+}, which is consistent with the element valence state of Ni 2p before the reaction (Fig. 5), and the position of the binding energy has hardly moved, indicating no qualitative changes appeared after reaction. Compared with the valence state before the reaction (Fig. 5), similar conclusions were achieved from other elements (manganese, copper, cobalt, iron, and aluminum). This can confirm the excellent stability of the HELOs again, which is consistent with the SEM results. The enhanced stability of HELOs also explains why the photo-assisted Zn-CO_2 batteries can continuously run for 42 h. The stability of high-entropy materials has also been reported on CO_2 transformations in Ref. [38], speculating that the superior stability of HELOs is usually due to their high entropy leading to their low Gibbs free energy [42, 43], which is the advantage of the high-entropy material itself.

The feasibility of the approach applied in this study for synthesizing high-entropy oxides was further verified. Based on above six-membered HELOs, other five-membered HELOs (MnCuCoFeAl-HELOs, NiCuCoFeAl-HELOs, NiMnCoFeAl-HELOs, NiMnCuFeAl-HELOs, NiMnCuCoAl-HELOs, and NiMnCuCoFe-HELOs) were synthesized by the identical method as the above six-membered HELOs. The basic characterization was carried out to validate the successful construction of five-membered HELOs. The crystal structures of the five-membered LDHs precursors and the five-membered HELOs were characterized by XRD patterns. As shown by the results in Fig. 12(a), the main diffraction peaks appearing at 11.6°, 23.3°, 34.7°, 39.2°, 46.7°, 60.3°, and 61.7° can be indexed to (003), (006), (012), (015), (018), (110), and (113) planes of the LDHs, respectively. The characteristic peaks all appear, and there is no obvious difference in the positions of diffraction peaks. There are only slight differences in the intensity of diffraction peaks, which is mainly influenced by different metal elements or is under the synergistic influence between the elements. Generally, the characteristic peaks are highly consistent with the crystal planes of LDHs, indicating that all the five-membered LDHs precursors were successfully prepared. Figure 12(b) exhibits the XRD patterns of the corresponding five-element HELOs, in which peaks located at 19.0°, 31.3°, 36.8°, 44.8°, and 65.23° are corresponding to the crystal planes (111), (220), (311), (400), and (440) of HELOs, respectively. Three obvious diffraction peaks (36.8°, 44.8°, and

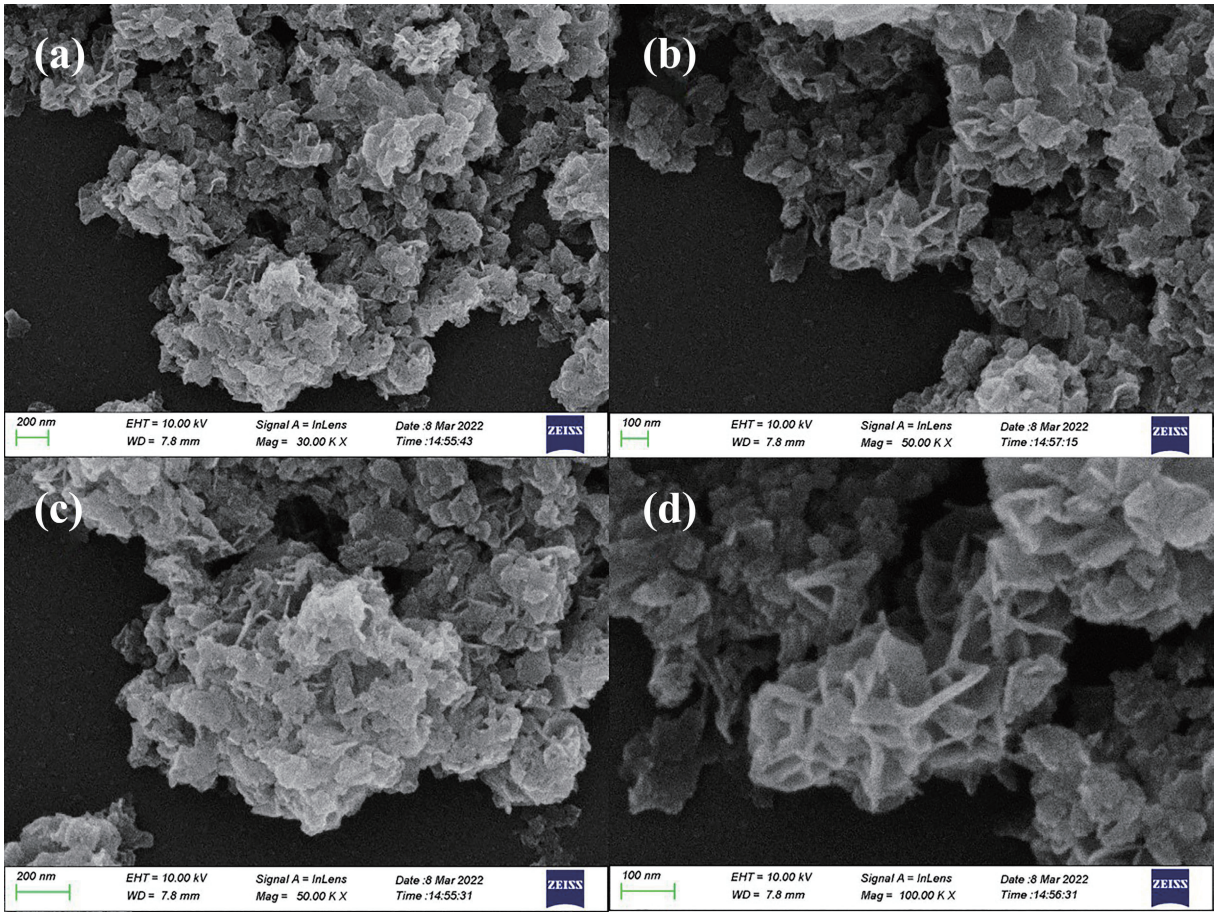

Figure 10 SEM images of HELOs after photoelectrochemical reduction of CO_2 with different magnifications.

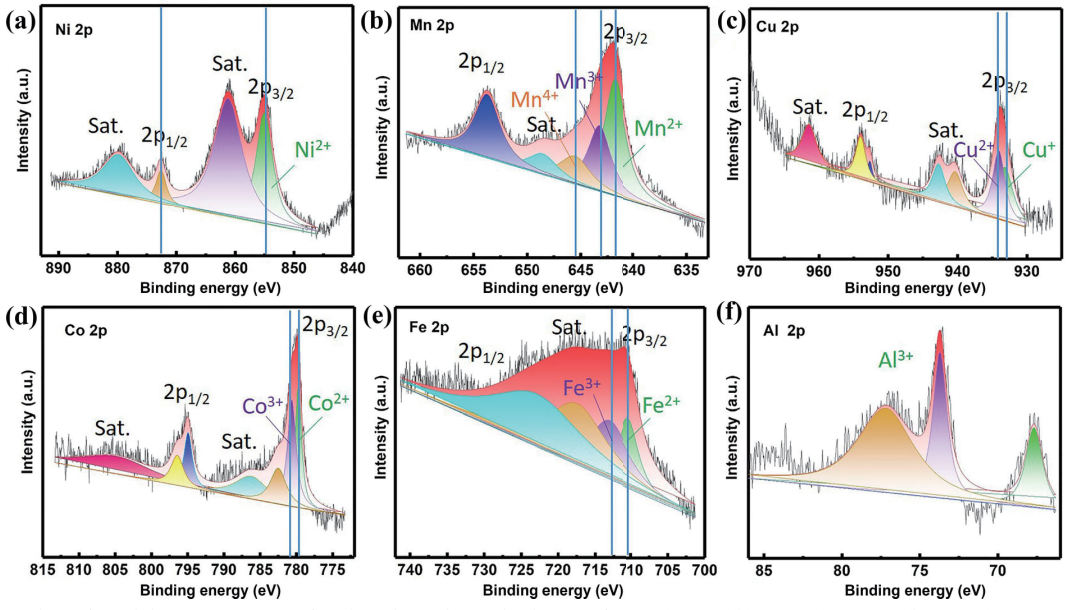

Figure 11 XPS analysis of metal elements in HELOs after photoelectrochemical reduction of CO_2: (a) Ni 2p, (b) Mn 2p, (c) Cu 2p, (d) Co 2p, (e) Fe 2p, and (f) Al 2p.

65.23°) appear in each five-element HELOs, while other characteristic peaks do not all appear, which is mainly ascribed to the influence of the scanning speed of XRD characterization and the poor crystallinity of the material itself. However, the appearance of three strong diffraction peaks and the existence of this single phase prove the successful construction of six kinds of five-element HELOs. In addition, SEM was performed to investigate the morphology and structure of five-membered HELOs. As shown in Figs. S2 and S3 in the ESM, all five-membered HELOs retain the lamellar structure resembling the LDHs precursors. Furthermore, element mapping was applied for investigating the elements dispersion of five-membered HELOs, and the results demonstrate that elements are uniformly distributed in each sample as displayed in Fig. S4 in the ESM. The above analysis elucidates that the method for preparing high-entropy oxides in this work is feasible and repeatable with different elements as well as provides a promising platform for the design and construction of high-entropy oxides. The precursor LDHs have been achieved by industrial production, so the scheme in this work is expected to become an avenue of industrial production of high-entropy oxides.

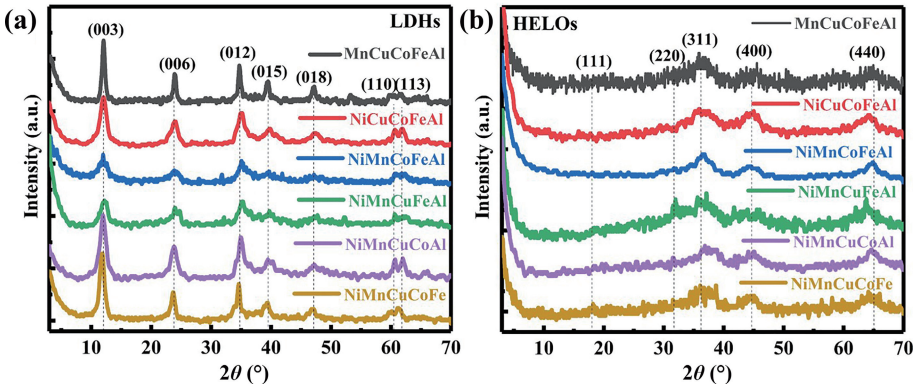

Figure 12 XRD patterns of (a) five-membered LDHs precursors and (b) five-membered HELOs.

4 Conclusions

In this work, HELOs were attained successfully by the strategy of calcination at a low temperature (300 ℃) under air atmosphere from the precursors of NiMnCuCoFeAl-LDHs. HELOs were employed for photoelectric conversion of CO_2 and in a photo-assisted Zn-CO_2 battery. Then, the yield and selectivity of photoelectric conversion of CO_2 were explored, and the charge–discharge voltage and long-term cycling stability of the photo-assisted Zn-CO_2 battery were investigated. For the photoelectric CO_2 reduction reaction, carbon monoxide is the main product, and the highest yield of 909.55 $\mu mol \cdot g^{-1} \cdot h^{-1}$ was obtained under −0.8 V vs. RHE, which is almost twice that of pure electrocatalysis. In addition, for Zn-CO_2 battery, the charging voltage of the battery was as high as 2.62 V, while it reduced to 2.40 V with the assistance of light; the discharging voltage is 0.51 V and increased to 0.59 V after illumination; hence, the round-trip efficiency of the battery was improved, indicating that illumination played a positive role in both charging process and discharging process. In addition, the long cycling stability was examined under constant capacity conditions, and the result demonstrates that battery can continuously run for 42 h under illumination conditions. In conclusion, this work not only opens a new avenue for the design and development of high-entropy materials but also broadens the preparation method of two-dimensional layered nanomaterials. It also expands the research of high-entropy oxides in the field of photoelectric catalysis and in the photo-assisted systems, which opens up ideas and lays a foundation for the research of high-entropy materials in the field of energy catalysis.

Acknowledgements

The authors express special gratitude for the financial support from the National Basic Research Program of China (No. 2014CB932101), the National Natural Science Foundation of China (Nos. 21571013 and 52073023) and Program for Chang Jiang Scholars and Innovative Research Team in University (No. IRT1205).

Electronic Supplementary Material: Supplementary material (HRTEM, SEM, element mapping, and EDS results) is available in the online version of this article at https://doi.org/10.1007/s12274-022-5259-5.

References

[1] Xu, S. Z.; Carter, E. A. Theoretical insights into heterogeneous (photo)electrochemical CO_2 reduction. *Chem. Rev.* **2019**, *119*, 6631–6669.

[2] White, J. L.; Baruch, M. F.; Pander III, J. E.; Hu, Y.; Fortmeyer, I. C.; Park, J. E.; Zhang, T.; Liao, K.; Gu, J.; Yan, Y. et al. Light-driven heterogeneous reduction of carbon dioxide: Photocatalysts and photoelectrodes. *Chem. Rev.* **2015**, *115*, 12888–12935.

[3] Xie, J. F.; Wang, Y. B. Recent development of CO_2 electrochemistry from Li-CO_2 batteries to Zn-CO_2 batteries. *Acc. Chem. Res.* **2019**, *52*, 1721–1729.

[4] Zhu, Z.; Shi, X. M.; Fan, G. L.; Li, F. J.; Chen, J. Photo-energy conversion and storage in an aprotic Li-O_2 battery. *Angew. Chem.* **2019**, *131*, 19197–19202.

[5] Zhu, D. D.; Zhao, Q. C.; Fan, G. L.; Zhao, S.; Wang, L. B.; Li, F. J.; Chen, J. Photoinduced oxygen reduction reaction boosts the output voltage of a zinc-air battery. *Angew. Chem.* **2019**, *131*, 12590–12594.

[6] Liu, X. R.; Yuan, Y. F.; Liu, J.; Liu, B.; Chen, X.; Ding, J.; Han, X. P.; Deng, Y. D.; Zhong, C.; Hu, W. B. Utilizing solar energy to improve the oxygen evolution reaction kinetics in zinc-air battery. *Nat. Commun.* **2019**, *10*, 4767.

[7] Guan, D. H.; Wang, X. X.; Li, M. L.; Li, F.; Zheng, L. J.; Huang, X. L.; Xu, J. J. Light/electricity energy conversion and storage for a hierarchical porous In_2S_3@CNT/SS cathode towards a flexible Li-CO_2 battery. *Angew. Chem., Int. Ed.* **2020**, *59*, 19518–19524.

[8] Li, Z.; Li, M. L.; Wang, X. X.; Guan, D. H.; Liu, W. Q.; Xu, J. J. *In situ* fabricated photo-electro-catalytic hybrid cathode for light-assisted lithium-CO_2 batteries. *Mater. Chem. A* **2020**, *8*, 14799–14806.

[9] Wang, X. Y.; Xie, J. F.; Ghausi, M. A.; Lv, J. Q.; Huang, Y. Y.; Wu, M. X.; Wang, Y. B.; Yao, J. N. Rechargeable Zn-CO_2 electrochemical cells mimicking two-step photosynthesis. *Adv. Mater.* **2019**, *31*, 1807807.

[10] Liu, X. Y.; Xiao, J. P.; Peng, H. J.; Hong, X.; Chan, K.; Nørskov, J. K. Understanding trends in electrochemical carbon dioxide reduction rates. *Nat. Commun.* **2017**, *8*, 15438.

[11] Peterson, A. A.; Nørskov, J. K. Activity descriptors for CO_2 electroreduction to methane on transition-metal catalysts. *J. Phys. Chem. Lett.* **2012**, *3*, 251–258.

[12] Bagger, A.; Ju, W.; Varela, A. S.; Strasser, P.; Rossmeisl, J. Electrochemical CO_2 reduction: A classification problem. *ChemPhysChem* **2017**, *18*, 3266–3273.

[13] Hussain, J.; Jónsson, H.; Skúlason, E. Calculations of product selectivity in electrochemical CO_2 reduction. *ACS Catal.* **2018**, *8*, 5240–5249.

[14] Pedersen, J. K.; Batchelor, T. A. A.; Bagger, A.; Rossmeisl, J. High-entropy alloys as catalysts for the CO_2 and CO reduction reactions. *ACS Catal.* **2020**, *10*, 2169–2176.

[15] Gao, Y.; Liu, Y. Z.; Yu, H. Y.; Zou, D. L. High-entropy oxides for catalysis: Status and perspectives. *Appl. Catal. A:Gen.* **2022**, *631*, 118478.

[16] Rost, C. M.; Sachet, E.; Borman, T.; Moballegh, A.; Dickey, E. C.; Hou, D.; Jones, J. L.; Curtarolo, S.; Maria, J. P. Entropy-stabilized oxides. *Nat. Commun.* **2015**, *6*, 8485.

[17] Yao, Y. G.; Dong, Q.; Brozena, A.; Luo, J.; Miao, J. W.; Chi, M. F.; Wang, C.; Kevrekidis, I. G.; Ren, Z. J.; Greeley, J. et al. High-entropy nanoparticles: Synthesis–structure–property relationships and data-driven discovery. *Science* **2022**, *376*, eabn3103.

[18] Li, T. Y.; Dong, Q.; Huang, Z. N.; Wu, L. P.; Yao, Y. G.; Gao, J. L.; Wang, X. Z.; Zhang, H. C.; Wang, D. W.; Li, T. et al. Interface engineering between multi-elemental alloy nanoparticles and a carbon support toward stable catalysts. *Adv. Mater.* **2022**, *34*, 2106436.

[19] Cui, M. J.; Yang, C. P.; Li, B. Y.; Dong, Q.; Wu, M. L.; Hwang, S.; Xie, H.; Wang, X. Z.; Wang, G. F.; Hu, L. B. High-entropy metal sulfide nanoparticles promise high-performance oxygen evolution reaction. *Adv. Energy Mater.* **2021**, *11*, 2002887.

[20] Wang, X. Z.; Dong, Q.; Qiao, H. Y.; Huang, Z. N.; Saray, M. T.; Zhong, G.; Lin, Z. W.; Cui, M. J.; Brozena, A.; Hong, M. et al. Continuous synthesis of hollow high-entropy nanoparticles for energy and catalysis applications. *Adv. Mater.* **2020**, *32*, 2002853.

[21] Li, T. Y.; Yao, Y. G.; Ko, B. H.; Huang, Z. N.; Dong, Q.; Gao, J. L.; Chen, W.; Li, J. G.; Li, S. K.; Wang, X. Z. et al. Carbon-supported high-entropy oxide nanoparticles as stable electrocatalysts for oxygen reduction reactions. *Adv. Funct. Mater.* **2021**, *31*, 2010561.

[22] Yao, Y. G.; Huang, Z. N.; Xie, P. F.; Lacey, S. D.; Jacob, R. J.; Xie, H.; Chen, F. J.; Nie, A. M.; Pu, T. C.; Rehwoldt, M. et al. Carbothermal shock synthesis of high-entropy-alloy nanoparticles. *Science* **2018**, *359*, 1489–1494.

[23] Qiao, H. Y.; Saray, M. T.; Wang, X. Z.; Xu, S. M.; Chen, G.; Huang, Z. N.; Chen, C. J.; Zhong, G.; Dong, Q.; Hong, M. et al. Scalable synthesis of high entropy alloy nanoparticles by microwave heating. *ACS Nano* **2021**, *15*, 14928–14937.

[24] Cui, M. J.; Yang, C. P.; Hwang, S.; Yang, M. H.; Overa, S.; Dong, Q.; Yao, Y. G.; Brozena, A. H.; Cullen, D. A.; Chi, M. F. et al. Multi-principal elemental intermetallic nanoparticles synthesized via a disorder-to-order transition. *Sci. Adv.* **2022**, *8*, eabm4322.

[25] Yao, Y. G.; Huang, Z. N.; Hughes, L. A.; Gao, J. L.; Li, T. Y.; Morris, D.; Zeltmann, S. E.; Savitzky, B. H.; Ophus, C.; Finfrock, Y. Z. et al. Extreme mixing in nanoscale transition metal alloys. *Matter* **2021**, *4*, 2340–2353.

[26] Zhang, Y. *High-Entropy Materials*: *A Brief Introduction*; Springer: Singapore, 2019; pp 215–232.

[27] Miracle, D. B.; Senkov, O. N. A critical review of high entropy alloys and related concepts. *Acta Mater.* **2017**, *122*, 448–511.

[28] George, E. P.; Raabe, D.; Ritchie, R. O. High-entropy alloys. *Nat. Rev. Mater.* **2019**, *4*, 515–534.

[29] Liu, L. Y.; Zhang, Y.; Han, J. H.; Wang, X. Y.; Jiang, W. Q.; Liu, C. T.; Zhang, Z. W.; Liaw, P. K. Nanoprecipitate-strengthened high-entropy alloys. *Adv. Sci.* **2021**, *8*, 2100870.

[30] Dong, Q.; Hong, M.; Gao, J. L.; Li, T. Y.; Cui, M. J.; Li, S. K.; Qiao, H. Y.; Brozena, A. H.; Yao, Y. G.; Wang, X. Z. et al. Rapid synthesis of high-entropy oxide microparticles. *Small* **2022**, *18*, 2104761.

[31] Zhao, C. L.; Ding, F. X.; Lu, Y. X.; Chen, L. Q.; Hu, Y. S. High-entropy layered oxide cathodes for sodium-ion batteries. *Angew. Chem., Int. Ed.* **2020**, *59*, 264–269.

[32] McCormick, C. R.; Schaak, R. E. Simultaneous multication exchange pathway to high-entropy metal sulfide nanoparticles. *J. Am. Chem. Soc.* **2021**, *143*, 1017–1023.

[33] Cavin, J.; Ahmadiparidari, A.; Majidi, L.; Thind, A. S.; Misal, S. N.; Prajapati, A.; Hemmat, Z.; Rastegar, S.; Beukelman, A.; Singh, M. R. et al. 2D high-entropy transition metal dichalcogenides for carbon dioxide electrocatalysis. *Adv. Mater.* **2021**, *33*, 2100347.

[34] Zhao, X. H.; Xue, Z. M.; Chen, W. J.; Wang, Y. Q.; Mu, T. C. Eutectic synthesis of high-entropy metal phosphides for electrocatalytic water splitting. *ChemSusChem* **2020**, *13*, 2038–2042.

[35] Lai, D. W.; Kang, Q. L.; Gao, F.; Lu, Q. Y. High-entropy effect of a metal phosphide on enhanced overall water splitting performance. *J. Mater. Chem. A* **2021**, *9*, 17913–17922.

[36] Zhang, L. J.; Cai, W. W.; Bao, N. Z.; Yang, H. Implanting an electron donor to enlarge the d–p hybridization of high-entropy (oxy)hydroxide: A novel design to boost oxygen evolution. *Adv. Mater.* **2022**, *34*, 2110511.

[37] Nellaiappan, S.; Katiyar, N. K.; Kumar, R.; Parui, A.; Malviya, K. D.; Pradeep, K. G.; Singh, A. K.; Sharma, S.; Tiwary, C. S.; Biswas, K. High-entropy alloys as catalysts for the CO_2 and CO reduction reactions: Experimental realization. *ACS Catal.* **2020**, *10*, 3658–3663.

[38] Akrami, S.; Murakami, Y.; Watanabe, M.; Ishihara, T.; Arita, M.; Fuji, M.; Edalati, K. Defective high-entropy oxide photocatalyst with high activity for CO_2 conversion. *Appl. Catal. B:Environ.* **2022**, *303*, 120896.

[39] Gu, K. Z.; Wang, D. D.; Xie, C.; Wang, T. H.; Huang, G.; Liu, Y. B.; Zou, Y. Q.; Tao, L.; Wang, S. Y. Defect-rich high-entropy oxide nanosheets for efficient 5-hydroxymethylfurfural electrooxidation. *Angew. Chem., Int. Ed.* **2021**, *60*, 20253–20258.

[40] He, S.; Somayaji, V.; Wang, M. D.; Lee, S. H.; Geng, Z. J.; Zhu, S. Y.; Novello, P.; Varanasi, C. V.; Liu, J. High entropy spinel oxide for efficient electrochemical oxidation of ammonia. *Nano Res.* **2022**, *15*, 4785–4791.

[41] Guo, H. X.; Wang, W. M.; He, C. Y.; Liu, B. H.; Yu, D. M.; Liu, G.; Gao, X. H. Entropy-assisted high-entropy oxide with a spinel structure toward high-temperature infrared radiation materials. *ACS Appl. Mater. Interfaces* **2022**, *14*, 1950–1960.

[42] Oses, C.; Toher, C.; Curtarolo, S. High-entropy ceramics. *Nat. Rev. Mater.* **2020**, *5*, 295–309.

[43] Wright, A. J.; Wang, Q. Y.; Huang, C. Y.; Nieto, A.; Chen, R. K.; Luo, J. From high-entropy ceramics to compositionally-complex ceramics: A case study of fluorite oxides. *J. Eur. Ceram. Soc.* **2020**, *40*, 2120–2129.